chemosensors

MDPI

Article

Conduction Mechanism in Lead Sulfide Quantum Dot Gas Sensors

Yanting Tang [1], Jingyao Liu [2], Bowen Zhou [2], Lanpeng Guo [2], Hua-Yao Li [2] and Huan Liu [2,*]

[1] School of Integrated Circuit (School of Artificial Intelligence), Beijing Polytechnic University, Beijing 100176, China; yantingtang@bpu.edu.cn
[2] School of Integrated Circuits, Huazhong University of Science and Technology, Wuhan 430074, China; liujingyao008@163.com (J.L.); zhoubowen202604@163.com (B.Z.); guolanpeng@hust.edu.cn (L.G.); huayaoli@hust.edu.cn (H.-Y.L.)
* Correspondence: huan@hust.edu.cn

Abstract

Colloidal quantum dots (CQDs) are ideal for room-temperature gas sensors due to their high surface area, abundant dangling bonds, and excellent film-forming properties. However, the underlying conduction mechanism remains unclear, lacking in-depth analysis of gas–solid charge transfer and carrier transport, which hinders the rational design of high-performance gas sensors. To address this, we fabricated a PbS colloidal quantum dot thin-film transistor (TFT) gas sensor that enables in situ analysis of carrier concentration and mobility via gate voltage modulation. We systematically measured the variations in conductivity, carrier concentration, and mobility with NO_2 concentration and established a normalized weight variation model. The results show that the conductivity increase upon NO_2 exposure is primarily due to the rise in carrier concentration induced by gas adsorption. At low concentrations (below 0.5 ppm), the response is dominated by mobility variation. This work provides a physically meaningful theoretical framework for understanding the conduction mechanism.

Keywords: semiconductor gas sensor; PbS colloidal quantum dots; field-effect transistor; conduction mechanism; normalized weight variation model

1. Introduction

Semiconductor gas sensors offer significant advantages such as high sensitivity, a wide range of detectable gases, and low cost, making them promising for applications in environmental monitoring, agricultural production, and medical diagnostics [1–4]. Their sensing performance is jointly determined by the receptor function and the transducer function. The receptor function is responsible for recognizing and adsorbing gas molecules, while the transducer function converts chemical signals into electrical signals [5,6]. Reducing the size of semiconductor materials to the nanoscale, particularly when the grain size is comparable to or smaller than the Debye length, can significantly enhance sensor performance. This grain size effect has been widely demonstrated [7,8].

Among various nanomaterials, lead sulfide colloidal quantum dots (PbS CQDs) have attracted considerable attention due to their unique physicochemical properties. PbS CQDs possess an extremely high surface-to-volume ratio and abundant surface dangling bonds, exhibiting excellent room-temperature gas-sensing performance [9,10]. Furthermore, their solution processability facilitates the fabrication of high-quality thin films, and their grain size (2–20 nm) is much smaller than the room-temperature Debye length [11], maximizing

Check for updates

Received: 15 May 2026
Revised: 1 June 2026
Accepted: 4 June 2026
Published: 7 June 2026

Copyright: © 2026 by the authors. Licensee MDPI, Basel, Switzerland. This article is an open access article distributed under the terms and conditions of the Creative Commons Attribution (CC BY) license.

the grain size effect. In recent years, significant progress has been made in gas sensors based on PbS CQDs, enabling room-temperature detection of various gases including NO_2, H_2S, NH_3, and CH_4 [12–15], with high sensitivity, fast response, and good stability.

However, despite the excellent performance of PbS CQD-based gas sensors, the underlying electronic transduction mechanism remains unexplained. Specifically, it refers to how the adsorption of gas molecules affects the carrier behavior inside the semiconductor and ultimately translates into a macroscopic electrical signal. For a long time, research has mostly focused on improving device performance [16,17], while systematic investigations on the intrinsic physical mechanisms are lacking. In particular, for highly confined nanocrystalline systems such as PbS CQDs, surface adsorbates not only alter the carrier concentration but may also significantly affect carrier mobility through surface scattering [18]. Nevertheless, the respective contributions of carrier concentration and mobility during gas response remain unexplored. This severely limits the rational design and performance optimization of semiconductor gas sensors. Fortunately, unlike traditional two-terminal resistive sensors, field-effect transistor devices utilize gate voltage modulation to independently control the carrier distribution in the channel and to extract two key parameters [19–21], namely carrier mobility and carrier concentration.

Based on this, this work constructs a PbS CQD thin film transistor (PbS CQD-TFT) gas sensor to systematically investigate how NO_2-induced charge transfer affects the electrical properties of quantum dot thin films. By establishing a normalized weight variation model of carrier concentration and mobility, combined with the flat-band theory, this study attempts to elucidate the respective contributions of carrier concentration and mobility during the conduction process, reveal the dynamic competition between surface scattering and doping effects, and clarify the conduction mechanism in quantum dot gas-sensing thin films from an energy band perspective.

2. Materials and Methods

2.1. Synthesis of PbS CQDs

PbS CQDs were synthesized using a hot-injection organic method. First, 0.45 g of PbO was added to a three-neck flask, followed by appropriate amounts of oleic acid and octadecene. The mixture was slowly heated to 90 °C under vacuum with continuous stirring for 6 h until the turbid yellow PbO solution turned into a clear, colorless lead oleate precursor solution. The atmosphere was then switched to nitrogen, and the temperature was gradually increased. A mixture of 140 μL of trimethylsilane and 10 mL of octadecene was rapidly injected into the lead oleate solution. The mixture turned black within seconds due to the nucleation and growth of PbS CQDs. Subsequently, the solid product was collected by centrifugation, alternately washed with acetone and toluene, and dried at 70 °C for 8 h. Finally, the product was dispersed in octane to prepare a 15 mg/mL PbS CQDs solution for use.

2.2. Fabrication of PbS CQDs TFT

PbS CQDs TFTs with a bottom-gate bottom-contact structure were fabricated on highly doped nitrogen silicon substrates, where SiO_2 served as both the back gate and the gate dielectric layer. Electrodes were first prepared using photolithography and electron beam evaporation. A 50 μL aliquot of the PbS CQDs solution was spin-coated onto the device surface, and solid-state ligand exchange was performed using $NaNO_2$ (7 mg mL^{-1} in methanol) and cetyltrimethylammonium bromide (10 mg mL^{-1} in methanol). This process was repeated twice. Finally, the devices were annealed at 60 °C for 10 min to obtain the PbS CQDs TFTs.

2.3. Gas Sensing Performance and In Situ Electrical Characterization

Gas sensing performance and in situ electrical measurements were conducted using a home-built in situ atmosphere probe station system. The tests were performed at room temperature using high-purity nitrogen as the carrier gas. NO_2 concentrations ranging from 0 to 5 ppm were prepared with a mass flow controller (MFC), and the total flow rate was kept constant at 0.5 L/min. Dry N_2 was introduced for a period of time to ensure a homogeneous atmosphere in the chamber. After the device current stabilized, the electrical characteristic curves were sequentially collected for each gas concentration. The measurement procedure for each concentration consisted of exposure to NO_2 atmosphere for 10 min, followed by N_2 purging for 17 min to allow desorption.

3. Results and Discussion

As schematically illustrated in Figure 1a, the PbS CQD solid film were used as both an active layer for gas sensing and a semiconductor channel layer for the fabricated bottom-gate bottom-contact PbS CQD-TFT structure. Figure 1b displays the cross-sectional SEM image of PbS CQD-TFT, confirming a film thickness of ~16 nm after spin-coating and ligand exchange procedure. Since the CQD diameter is much smaller than its exciton Bohr radii and Debye length at room temperature, grain-size effect can significantly contribute to gas sensing, and the electronic transduction mechanism of CQD-based gas sensors will be worth exploring. Meanwhile, the ratio of the thickness of CQD thin film to its Debye length is comparable or even smaller, and the role of surface scattering in charge carrier mobility should not be neglected. Surface scattering could be influenced by the absorbed species and this could influence carrier mobility, which is associated with the transducer function and thus affects the overall conduction process.

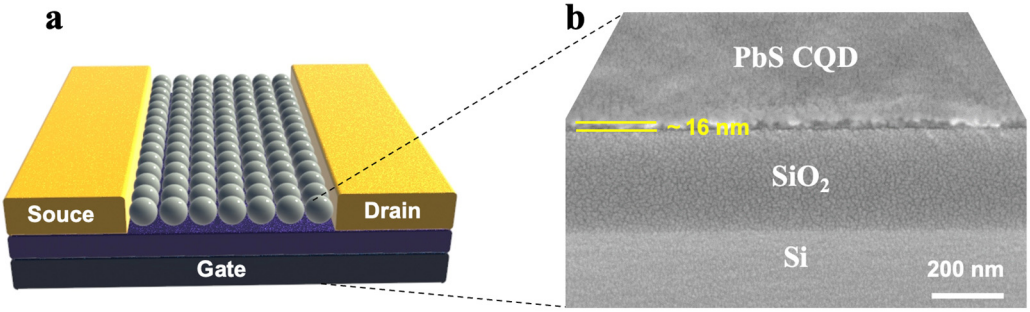

Figure 1. (**a**) Schematic diagram of the PbS CQD-TFT device structure; (**b**) cross-sectional SEM image of the PbS CQD-TFT.

The electrical characteristics of the PbS CQD-TFT was first measured under ambient air conditions. The almost symmetric current–voltage characteristic (I-V) is shown in Figure 2a, which indicates that the Cr/Au electrodes with a low work function could form good ohmic contacts with CQD film. Figure 2b,c display the representative output (I_D-V_{DS}) and transfer (I_D-V_G) characteristics of our PbS CQD-TFT under gate bias (V_G) conditions and demonstrates that the drain current (I_D) increased with the increase in the negative V_G, exhibiting well-behaved p-type current modulations. A schematic diagram of the PbS CQD-TFT structure is also depicted in the inset of Figure 2c. Furthermore, from the trend of the forward- and reverse-sweep transfer curves (Figure 2d), the device exhibits a clear current hysteresis, which is presumably related to the abundant surface dangling bonds of the quantum dots as well as the water/oxygen defect states introduced during film deposition. The presence of these surface defect states affects the electron-hole recombination probability, prolongs the carrier relaxation time, introduces a certain capacitive effect in the channel, and thus gives rise to the current hysteresis.

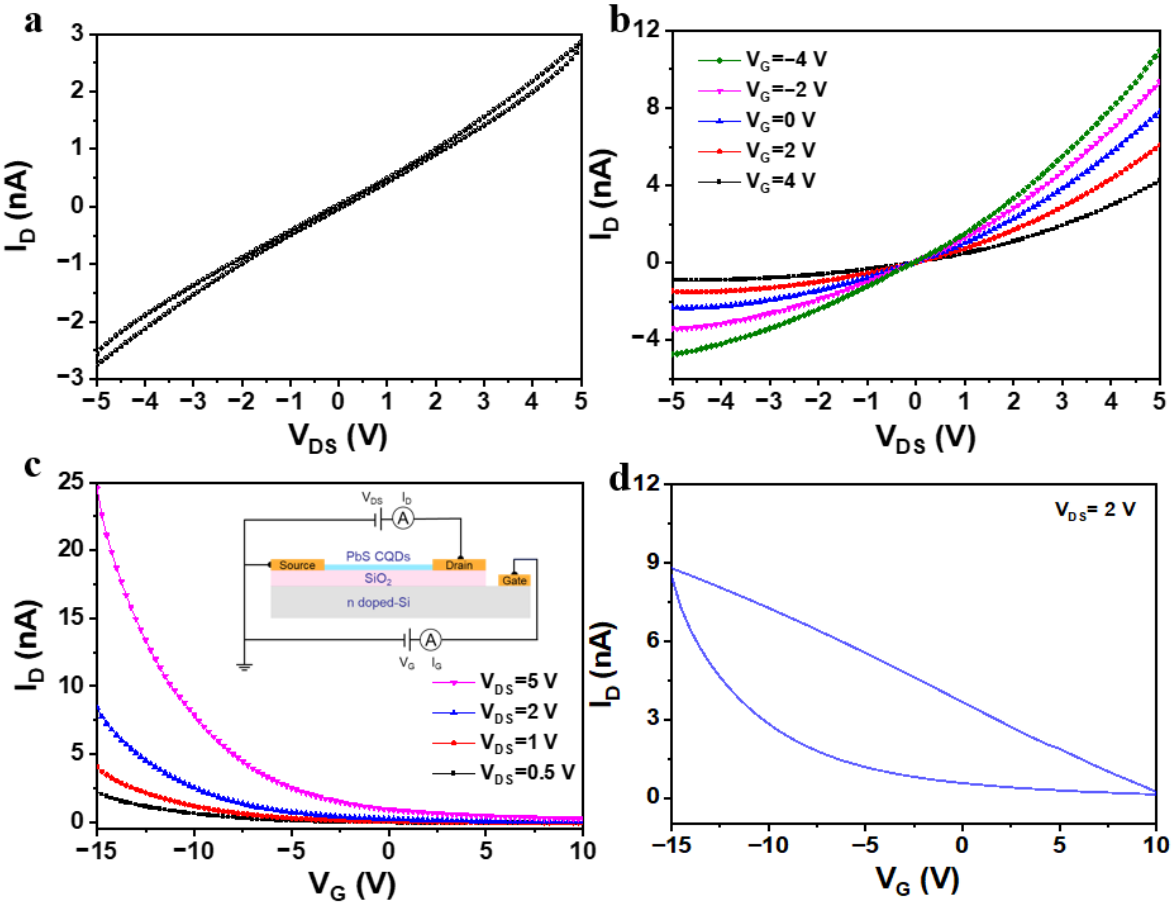

Figure 2. Electrical characterization of the PbS CQD-TFT in ambient air. (**a**) Current–voltage characteristic curve; (**b**) output characteristic curves under different gate biases; (**c**) transfer characteristic curves under different source–drain voltages; (**d**) transfer characteristic curves at a source–drain voltage of 2 V.

We continued to characterize the in situ electrical properties of the p-type conductive PbS CQD solids in a NO_2 atmosphere. Figure 3a shows the real-time current response of the device under different NO_2 concentrations. Upon exposure to NO_2, the current increases. This increase is attributed to electron transfer from PbS CQDs to NO_2 molecules, which induces p-type doping and thus enhances the conductivity of the p-type PbS CQD film. Moreover, the current recovers to near its initial value after NO_2 is removed, confirming stable, reversible, and concentration-dependent sensing behavior of the PbS CQDs. Furthermore, the electrical characteristics of the PbS CQD-TFT exposed to NO_2 concentrations ranging from 0 to 5 ppm were measured at room temperature. The curves at each concentration were then extracted to form a combination of I I-V, I_D-V_{DS} (V_G = −4 V) and I_D-V_G (V_{DS} = 2 V) curves with gas concentration information, as illustrated in Figure 3b–d.

Because all measurements under different NO_2 concentrations were performed on the same device under identical electrical conditions, the influence of contact resistance remains essentially constant across different gas concentrations. For the output characteristic curves (Figure 3c), the bias conditions are constant. Therefore, the increase in I_D with NO_2 concentration in these measurements arises solely from the gas–solid interaction. For the transfer characteristic curves (Figure 3d), the gate voltage is scanned, but the same V_G range was used for all NO_2 concentrations. Consequently, the concentration-dependent variation in the extracted μ_p reflects the influence of NO_2 adsorption on the channel properties.

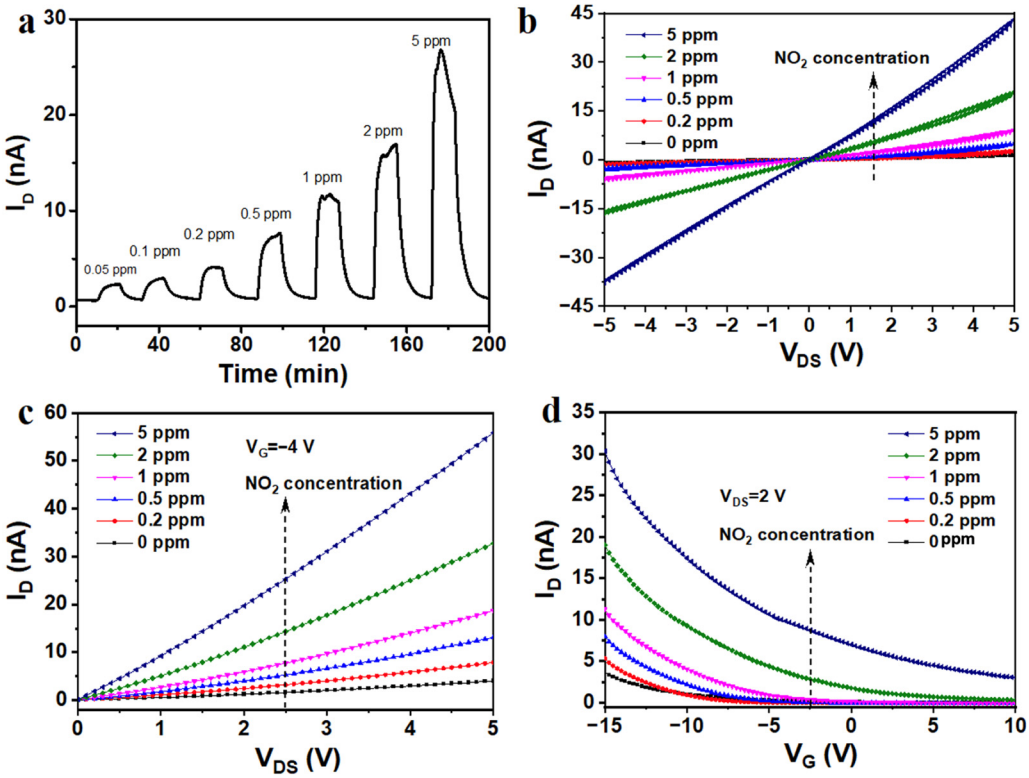

Figure 3. Electrical measurement curves of the PbS CQD-TFT under different NO_2 atmospheres. (**a**) Real-time gas sensing response curves; (**b**) current-voltage characteristic curves; (**c**) output characteristic curves (V_G = −4 V); (**d**) transfer characteristic curves (V_{DS} = 2 V).

According to the I-V characteristics of PbS CQD-TFT, the detailed electrical parameters including resistance (R), conductivity (σ), carrier mobility (μ_p) and carrier concentration (p_0) in a gas atmosphere can be extracted using the following Equations (1)–(3):

$$R = \frac{L}{\sigma S} \quad (1)$$

$$\mu_p = \frac{dI_D}{dV_G} \cdot \frac{L}{WC_iV_{DS}} \quad (2)$$

$$\sigma = p_0 q \mu_p \quad (3)$$

where L and W are the channel length and width, S is the cross-section area for the flow of current, dI_D/dV_G is the slope of the I_D-V_G transfer curve in the linear regime, C_i is the dielectric capacitance per unit area, V_{DS} is the drain voltage, and q is the electronic charge.

It is worth noting that the extracted mobility μ_p from Equation (2) represents the effective field-effect mobility. However, its relative change upon gas exposure provides physically meaningful insight into molecular adsorption-induced scattering, as parasitic factors remain constant under identical bias conditions on the same device. Moreover, current hysteresis was observed in the transfer curves under ambient air (Figure 2d). Here, to ensure comparability across different NO_2 concentrations, all mobility values were extracted exclusively from the forward gate sweep (from positive to negative gate bias). This consistent sweep direction minimizes the influence of hysteresis and trap-filling effects on mobility extraction.

The changes in σ, μ_p and p_0 with different concentrations of NO_2 were further plotted in Figure 4a–c. As the NO_2 concentration increases, these three parameters increased simultaneously and showed a certain functional relation with gas concentrations, respectively. On one hand, acceptor-like doping caused by the adsorption of NO_2 molecules on

the surface of PbS CQDs resulted in an increase in the injected hole concentration; thus, the carrier concentration monotonically increased with the increase in gas concentration (Figure 4b). Further, the computed binding energy of NO_2 molecules on the PbS CQD surface was much stronger than O_2 [9], indicating that NO_2 preferentially adsorbs and accepts electrons to form NO_2^- while injecting holes into the PbS CQDs and likely displacing pre-adsorbed oxygen species. Although the negatively charged NO_2^- itself acts as an additional Coulomb scattering center, the substantial increase in hole concentration can induce dynamic screening of ionized impurity scattering in this heavily doped regime [22,23], thereby partially offsetting the extra scattering introduced by NO_2^- and leading to an increased net mobility. Therefore, a notable improvement in the mobility of the p-type PbS CQD film can be observed upon NO_2 gas injection (Figure 4c). However, when exposed to high concentrations of NO_2 gas, the hole concentration increased significantly, and the impact of ionized impurity scattering became more significant as well; thus, the increase in hole mobility was limited and eventually leveled off.

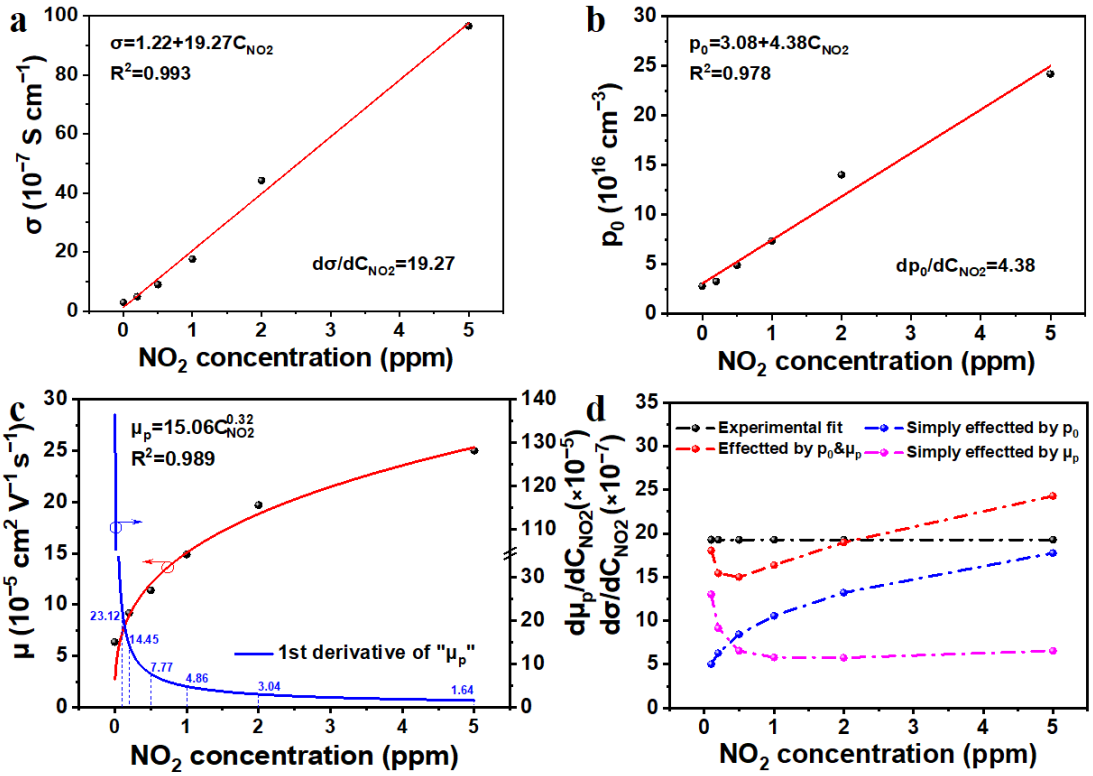

Figure 4. (**a**) Variation and functional relationship of the conductivity of the PbS CQD film with gas concentration; (**b**) variation and functional relationship of the carrier concentration of the PbS CQD film with gas concentration; (**c**) variation and functional relationship of the mobility of the PbS CQD film with gas concentration; (**d**) first-derivative relationship of the carrier concentration and mobility of the PbS CQD film with respect to gas concentration, and their influence on the first derivative of conductivity.

From Equation (3), it can be seen that the change in σ results from μ_p and p_0, and they have a certain functional relationship with NO_2 concentration (C_{NO2}), respectively. We thus proposed to investigate the effects of μ_p and p_0 on σ with changes in C_{NO2} by taking the derivative, as shown in Equation (4):

$$\frac{d\sigma}{dC_{NO2}} = \frac{dp_0}{dC_{NO2}} q\mu_p + p_0 q \frac{d\mu_p}{dC_{NO2}} \quad (4)$$

Because of the fairly high goodness-of-fit of σ-C_{NO2} and p_0-C_{NO2} obtained by linear fitting, their first derivatives correspond to the slopes of the fitting curves, giving $d\sigma/dC_{NO2}$ and dp_0/dC_{NO2} as 19.27×10^{-7} and 4.38×10^{16}, respectively, while μ_p-C_{NO2} was more suitably fitted by a power function with a power index of 0.32 (see red line in Figure 4c) so that the first derivative of μ_p-C_{NO2} also follows a power function (see blue line in Figure 4c). The parameters at various NO_2 concentrations were taken from Equation (4), and the effects of μ_p and p_0 on σ could be obtained qualitatively (Figure 4d). The blue and pink lines represent the effects of p_0 (without regard to μ_p) and μ_p (without regard to p_0) on σ, respectively. With the increase in NO_2 concentration, the blue line tends toward the black line, which was the experimental fitting value of $d\sigma/dC_{NO2}$ calculated from Figure 4a. In this case of relatively high NO_2 concentration, it can be approximately considered that the effect on σ was mainly caused by p_0, while the effect of μ_p is relatively small. In contrast, at low concentrations (below 0.5 ppm), μ_p did have a significant impact on σ that could not be negligible. We also took into consideration the joint effects of μ_p and p_0 on σ. As the R-squared values of σ-C_{NO2}, μ_p-C_{NO2} and p_0-C_{NO2} fitting functions cannot be exactly 1, errors exist inevitably, and the value of $d\sigma/dC_{NO2}$ calculated from Equation (4) (red line) does not exactly coincide with the constant value of $d\sigma/dC_{NO2}$ (black line) obtained from the slope of the fitting curve of σ-C_{NO2}. However, it could be roughly estimated that the integral values of the two lines may be very close.

Thanks to the constructed air-stable and NO_2-sensitive PbS CQD-TFT with the feature of electrical parameter extraction, we were able to further investigate the influence of nitrogen dioxide gas on the electrical characteristics of the quantum dot film. We first established the normalized weight change model to clarify the above effects of μ_p and p_0 on σ with the change in C_{NO2} (Figure 5). The normalized weights of μ_p and p_0 are defined as:

$$W_{\mu_p}(C) = \frac{|p_0 q \frac{d\mu_p}{dC}|}{|\frac{dp_0}{dC} q\mu_p| + |p_0 q \frac{d\mu_p}{dC}|} \quad (5)$$

$$W_{p_0}(C) = \frac{|\frac{dp_0}{dC} q\mu_p|}{|\frac{dp_0}{dC} q\mu_p| + |p_0 q \frac{d\mu_p}{dC}|} \quad (6)$$

where $W_{\mu_p}(C)$ and $W_{p_0}(C)$ are the normalized contribution weights of μ_p and p_0 to $d\sigma/dC$, respectively.

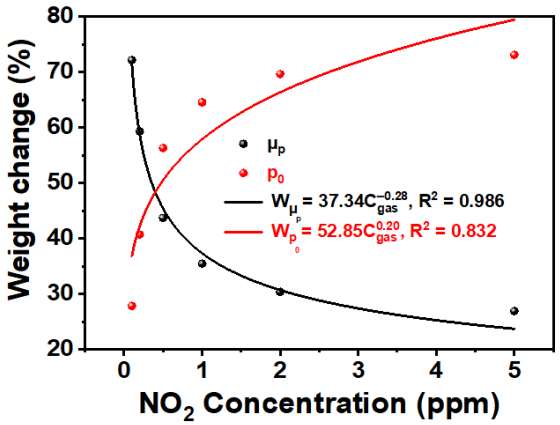

Figure 5. Normalized weight variation relationship of carrier concentration and mobility of the PbS CQD film with respect to conductivity.

After normalization, the sum of the weights of μ_p and p_0 equals 1 over the NO_2 concentration range of 0 to 5 ppm. The concentration dependence of each weight was fitted

by a power function, reflecting how the weights vary with increasing NO_2 concentration. The results of the weight change model show that the weight of μ_p on σ is relatively high at low gas concentrations, e.g., about 60% at 0.2 ppm NO_2, while p_0 plays a dominant role at high gas concentrations, e.g., about 73% at 5 ppm NO_2. It should be noted that the above weight results are semi-quantitative estimates obtained under specific fitting models (linear fit for p_0 vs. C_{NO2}, power-law fit for μ_p vs. C_{NO2}), primarily reflecting the relative trends of the two mechanisms with concentration, namely that mobility dominates at low concentrations while carrier concentration dominates at high concentrations.

Actually, the effect of μ_p on σ could not be ignored, especially at low gas concentrations. This also confirmed the reported literature [18] stating that for small grains, when the mean free path of free charge carriers becomes comparable with the dimension of the grains, the influence of surface scattering induced by absorbed species on mobility should be taken into consideration, which may further influence conductivity. Moreover, as the thickness of the CQD layer was comparable to the Debye length, the influence of surface phenomena may extend to the whole layer, and the surface scattering could also contribute in a significant way to mobility, especially under the absorbed gas species. As the concentration increased (above 1 ppm), acceptor-like surface state doping caused by NO_2 molecules led to a sharp increase in Δp_0, and the weight of p_0 gradually increased and played a dominant role in the weight change model. Actually, the increase in Δp_0 also increased the surface scattering probability of the impurity ions in the system, limiting the increase in μ_p and finally leading to a mild trend, thereby leading to a reduction in its weight value after normalization. The weight change functions of μ_p and p_0 on σ within the NO_2 concentration range could also be described by the fitted power function, respectively. The joint effects of μ_p and p_0 on σ over the whole concentration range could be revealed by the developed method, which further elucidates the origin of the gas-sensing effect from the perspective of the conduction mechanism.

We further established a complete depletion model with a flat-band diagram to elucidate the transducer function in PbS CQD gas sensors. Generally, large-size PbS nanocrystals (NCs) synthesized in an inert atmosphere always exhibit n-type conductive behavior [24,25], and the energy band structure is shown in Figure 6a. However, once exposed to ambient air, a large number of water and oxygen acceptor-like surface states will adsorb on the surface of NCs, resulting in the energy band bending at the gas–solid interface (Figure 6b), and surface depletion layers are formed and potential barriers are generated to some extent.

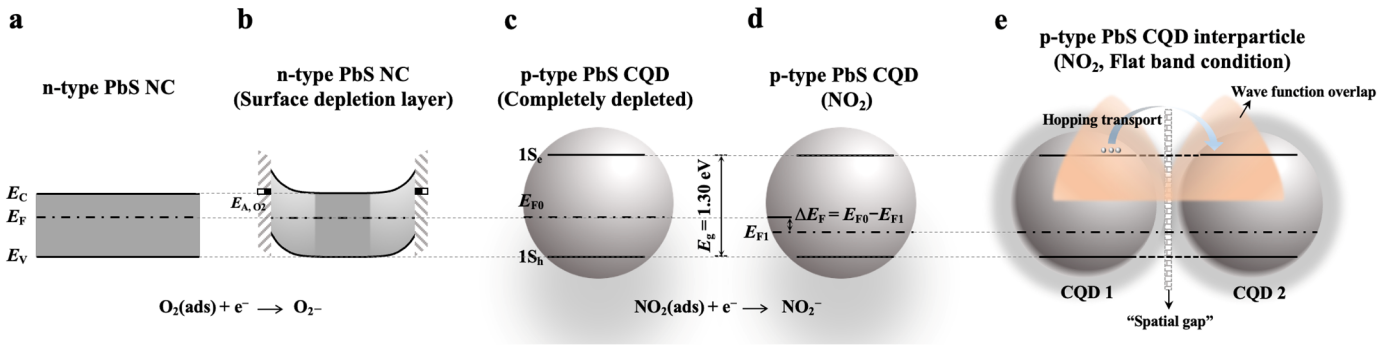

Figure 6. (**a**) Energy band diagram of a typical n-type PbS nanocrystal (NC) synthesized in an inert environment; (**b**) surface band bending of the n-type PbS NC under ambient air, where oxygen molecules act as acceptor-like surface states; (**c**) Flat-band energy diagram of the p-type PbS colloidal quantum dot (CQD) under ambient air; (**d**) Flat-band energy diagram under NO_2 exposure, showing the Fermi level shift (moving closer to the valence-band maximum, VBM); (**e**) Schematic of the hopping transport process between adjacent CQDs.

The NC size can be reduced to a few nanometers by controllable synthesis method to form CQD, whose grain size is much smaller than its exciton Bohr radii and Debye length. In this case, complete grain depletion and a flat-band condition can be assumed for almost each CQD and there are no surface barriers for inter-CQD or gas–solid interface charge transport since the electrons are squeezed out from the whole crystal to be supplied to the surface [26]. The solution-processed CQDs were synthesized in an inert environment and then deposited to form a conductive thin-film channel by the spin-coating method under air conditions. Due to the significant surface effect and strong grain size effect with such high-specific-surface CQDs, chemisorption-induced oxygen acceptor-like surface states can induce p-type doping and the whole CQD film becomescompletely depleted until the p-type inversion layer emerges, which is consistent with the above results of I-V characteristics and gas sensing behavior. Compared to NCs, the energy band width widens with the decrease in the CQD size and the final energy band structure of PbS CQD under air is depicted in Figure 6c. Upon exposure to the oxidizing gas NO_2, an accumulated hole concentration occurs in the p-type PbS CQD solids [27]. This disturbs the initial equilibrium in ambient air, causing the Fermi level to move from E_{F0} to E_F (Figure 6d), which is much closer to the valence-band maximum (VBM), corresponding to the increase in conductivity of the CQD film.

Furthermore, we discussed the carrier transport mechanism in CQD solids after the success of charge transfer at the gas–solid interface. As illustrated in Figure 6e, the adjacent CQD was used for detailed elucidation. The long oleate ligands introduced during synthesis form a tightly bound shell fully protecting the CQDs surface, which enables the individual CQD with good independence and dispersibility, but reduces the capacity of charge carrier transport as well. By the strategy of ligand exchange treatment, most oleate ligands were removed by short-chain ligands, reducing the interparticle distance and achieving strong coupling in CQD solids, thereby improved the transport behavior of charge carriers [28].

However, the "spatial gap" still remains between adjacent CQD to hinder carrier transport. In this case, the overlap of electronic wavefunctions of individual CQD can develop extended electronic states delocalized across multiple CQDs [29], leading to fast exciton diffusion or even tunneling between adjacent CQDs [11]. Moreover, strong wave function leakage outside the CQD core suggests that their macroscopically measured electronic properties could sensitively reflect changes at their surface [30], facilitating an excellent response upon the presence of specific gases. Based on the established flat-band energy diagram, we suggested that the charge carriers induced by charge transfer at the gas–solid interface may undergo a hopping transport process under the strong wave function overlap. Based on the above flat-band energy model, it can be reasonably inferred that after the gas–solid interfacial charge transfer between the quantum dots and NO_2 molecules, the charge carriers undergo conduction-band-to-conduction-band (or valence-band-to-valence-band) transitions under the strong interaction arising from the superposition of PbS CQD wavefunctions, thereby completing the electron transport process within the quantum dot film.

As a consequence of the gas–solid surface interaction, charge transfer takes place between the NO_2 molecules and the PbS CQD solids, and then the change in carrier concentration and mobility is translated into a change in the overall conductance inside the solids through the receptor and transducer functions, which is finally converted into a measurable electrical signal to complete the sensing process. The quantitative experimental approach of the CQD-TFT gas sensor paves the way not only for a fundamental understanding of the conduction mechanism for various nanocrystalline semiconductors, but also for developing Si-compatible sensor design principles, facilitating the development and innovation of semiconductor gas sensors.

4. Conclusions

This study has constructed a normalized weight variation model of carrier concentration and mobility based on the PbS CQD-TFT device platform, aiming to clarify the electrical origin of the gas-sensing effect from the perspective of conduction mechanism. Through analysis of the electrical parameters within the NO_2 concentration range, the transduction mechanism was elucidated, showing that it is dominated by mobility at low concentrations and by carrier concentration at high concentrations, verifying the dynamic competition between surface scattering and doping effects during the electronic transduction process. Furthermore, combined with the flat-band model, the conduction mechanism in the quantum dot gas-sensing film is further clarified, providing a physically interpretable theoretical framework for understanding charge transport in nanocrystal semiconductor gas sensors. It is expected that future work will employ independent characterization techniques such as temperature-dependent Hall effect, four-probe conductivity, or Kelvin probe force microscopy, which would help directly validate the decoupled variations in carrier concentration and mobility observed in this study. This work also offers new insights for the material design and device optimization of high-performance gas sensors.

Author Contributions: Conceptualization, H.L., H.-Y.L. and Y.T.; methodology, Y.T., H.-Y.L., L.G. and J.L.; validation, Y.T., L.G. and B.Z.; formal analysis, Y.T., B.Z. and H.-Y.L.; investigation, Y.T. and L.G.; data curation, Y.T., B.Z. and J.L.; writing—original draft preparation, Y.T.; writing—review and editing, Y.T. and H.L.; supervision, H.L. All authors have read and agreed to the published version of the manuscript.

Funding: This research was supported by the National Natural Science Foundation of China (No. 61922032, No. 62271222) and the Hubei Provincial Natural Science at Foundation of China (No. 2022CFA035). We thank funding support from National Key Research and Development Program of Hubei (2024BCB042), and Interdisciplinary Research Program of HUST (No. 5003190015). We also thank "Chutian Talent Program" Science and Technology Innovation Team of Hubei and the Analytical and Testing Center of Hust for support.

Institutional Review Board Statement: Not applicable.

Informed Consent Statement: Not applicable.

Data Availability Statement: The original contributions presented in this study are included in the article. Further inquiries can be directed to the corresponding author.

Conflicts of Interest: The authors declare no conflicts of interest.

References

1. Kaur, N. Nickel Oxide Nanostructures for Gas Sensing: Recent Advances, Challenges, and Future Perspectives. *ACS Sens.* **2025**, *10*, 1641–1674. [CrossRef]
2. Kumar, A.; Mazumder, J.T.; Joyen, K.; Favier, F.; Mirzaei, A.; Kim, J.-Y.; Kwoka, M.; Bechelany, M.; Jha, R.K.; Kumar, M.; et al. Defect engineering approaches for metal oxide semiconductor-based chemiresistive gas sensing. *Coord. Chem. Rev.* **2025**, *541*, 216836. [CrossRef]
3. Mandal, S.; Marsh, A.V.; Faber, H.; Ghoshal, T.; Goswami, D.K.; Tsetseris, L.; Heeney, M.; Anthopoulos, T.D. A robust organic hydrogen sensor for distributed monitoring applications. *Nat. Electron.* **2025**, *8*, 343–352. [CrossRef]
4. Song, J.; Kim, D.-H.; Tiepelt, J.; Jo, Y.-M.; McGrath, G.; Song, M.; Chen, T.; Wang, J.; Coto, A.; Palani, S.; et al. Tunable and highly sensitive functionalized carbon-nanotube-based integrated systems for chemical gas sensing. *Nat. Sens.* **2026**, *1*, 252–260. [CrossRef]
5. Yamazoe, N. New approaches for improving semiconductor gas sensors. *Sens. Actuators B Chem.* **1991**, *5*, 7–19. [CrossRef]
6. Yamazoe, N. Toward innovations of gas sensor technology. *Sens. Actuators B Chem.* **2005**, *108*, 2–14. [CrossRef]
7. Gillet, M.; Aguir, K.; Bendahan, M.; Mennini, P. Grain size effect in sputtered tungsten trioxide thin films on the sensitivity to ozone. *Thin Solid Film.* **2005**, *484*, 358–363. [CrossRef]

8. Han, M.A.; Kim, H.-J.; Lee, H.C.; Park, J.-S.; Lee, H.-N. Effects of porosity and particle size on the gas sensing properties of SnO_2 films. *Appl. Surf. Sci.* **2019**, *481*, 133–137. [CrossRef]
9. Liu, H.; Li, M.; Voznyy, O.; Hu, L.; Fu, Q.; Zhou, D.; Xia, Z.; Sargent, E.H.; Tang, J. Physically flexible, rapid-response gas sensor based on colloidal quantum dot solids. *Adv. Mater.* **2014**, *26*, 2718–2724. [CrossRef]
10. Farahmandpour, M.; Sadeghfar, F.; Asfaram, A.; Ghaedi, M.; Javadian, H. Improving the sensitivity and detection speed of methane gas at room temperature using a nanosensor based on lead sulfide (PbS) colloidal quantum dots. *Results Chem.* **2025**, *18*, 102760. [CrossRef]
11. Kagan, C.R.; Lifshitz, E.; Sargent, E.H.; Talapin, D.V. Building devices from colloidal quantum dots. *Science* **2016**, *353*, aac5523. [CrossRef]
12. Tang, Y.; Zhou, B.; Liu, J.; Chen, X.; Wang, H.; Hu, Z.; Mao, R.; Xing, Y.; Li, H.Y.; Li, D.; et al. Dual-Gate Modulation in a Quantum Dots/MoS_2 Thin-Film Transistor Gas Sensor. *ACS Sens.* **2025**, *10*, 320–328. [CrossRef]
13. Li, M.; Zhou, D.; Zhao, J.; Zheng, Z.; He, J.; Hu, L.; Xia, Z.; Tang, J.; Liu, H. Resistive gas sensors based on colloidal quantum dot (CQD) solids for hydrogen sulfide detection. *Sens. Actuators B Chem.* **2015**, *217*, 198–201. [CrossRef]
14. Liu, Y.; Wang, H.; Yang, S.; Chen, K.; Yang, T.; Wei, J.; Tian, J.; Chen, W. ppb level ammonia detection of 3D PbS quantum dots/reduced graphene oxide nanococoons at room temperature and Schottky barrier modulated behavior. *Sens. Actuators B Chem.* **2018**, *255*, 2979–2987. [CrossRef]
15. Roshan, H.; Mosahebfard, A.; Sheikhi, M.H. Effect of Gold Nanoparticles Incorporation on Electrical Conductivity and Methane Gas Sensing Characteristics of Lead Sulfide Colloidal Nanocrystals. *IEEE Sens. J.* **2018**, *18*, 1940–1945. [CrossRef]
16. Kwon, J.; Ha, Y.; Choi, S.; Jung, D.G.; An, H.K.; Kong, S.H.; Jung, D. Solution-processed NO_2 gas sensor based on poly(3-hexylthiophene)-doped PbS quantum dots operable at room temperature. *Sci. Rep.* **2024**, *14*, 20600. [CrossRef]
17. Bai, J.; Shen, Y.; Li, A.; Wu, M.; Xiao, H.; Zhao, Q.; Zhao, S.; Liu, W.; Cui, B. Design of PbS quantum dots–$PbMoO_4$–MoS_2 ternary nanocomposites for highly selective NO_2 sensing at room temperature. *Int. J. Miner. Metall. Mater.* **2025**, *32*, 1771–1782. [CrossRef]
18. Barsan, N.; Weimar, U. Conduction Model of Metal Oxide Gas Sensors. *J. Electroceram.* **2001**, *7*, 143–167. [CrossRef]
19. Shi, L.; Tang, P.; Hu, J.; Zhang, Y. A Strategy for Multigas Identification Using Multielectrical Parameters Extracted from a Single Carbon-Based Field-Effect Transistor Sensor. *ACS Sens.* **2024**, *9*, 3126–3136. [CrossRef] [PubMed]
20. Torsi, L.; Dodabalapur, A.; Sabbatini, L.; Zambonin, P. Multi-parameter gas sensors based on organic thin-film-transistors. *Sens. Actuators B Chem.* **2000**, *67*, 312–316. [CrossRef]
21. Hayasaka, T.; Lin, A.; Copa, V.C.; Lopez, L.P., Jr.; Loberternos, R.A.; Ballesteros, L.I.M.; Kubota, Y.; Liu, Y.; Salvador, A.A.; Lin, L. An electronic nose using a single graphene FET and machine learning for water, methanol, and ethanol. *Microsyst. Nanoeng.* **2020**, *6*, 50. [CrossRef]
22. Gong, J.; Zhang, C.; Hu, W.; Zhou, J.-J. Free-carrier screening unlocks high electron mobility in ultrawide bandgap semiconductor $CaSnO_3$. *Appl. Phys. Lett.* **2025**, *127*, 092110. [CrossRef]
23. Rode, D.L.; Cetnar, J.S. Electron mobility of heavily doped semiconductors including multiple scattering by ionized impurities. *J. Appl. Phys.* **2023**, *134*, 075701. [CrossRef]
24. Oh, S.J.; Berry, N.E.; Choi, J.H.; Gaulding, E.A.; Lin, H.; Paik, T.; Diroll, B.T.; Muramoto, S.; Murray, C.B.; Kagan, C.R. Designing high-performance PbS and PbSe nanocrystal electronic devices through stepwise, post-synthesis, colloidal atomic layer deposition. *Nano Lett.* **2014**, *14*, 1559–1566. [CrossRef]
25. Ning, Z.; Voznyy, O.; Pan, J.; Hoogland, S.; Adinolfi, V.; Xu, J.; Li, M.; Kirmani, A.R.; Sun, J.P.; Minor, J.; et al. Air-stable n-type colloidal quantum dot solids. *Nat. Mater.* **2014**, *13*, 822–828. [CrossRef]
26. Liu, J.; Lv, J.; Shi, J.; Wu, L.; Su, N.; Fu, C.; Zhang, Q. Size effects of tin oxide quantum dot gas sensors: From partial depletion to volume depletion. *J. Mater. Res. Technol.* **2020**, *9*, 16399–16409. [CrossRef]
27. Tang, Y.; Zhou, B.; Liu, J.; Guo, L.; Ying, B.; Chen, X.; Zhang, W.; Liang, Y.; Li, L.; Duan, Q.; et al. Specific Odor Coding Using a Single Thin-Film Transistor. *Nano Lett.* **2025**, *25*, 7587–7594. [CrossRef] [PubMed]
28. Kagan, C.R.; Murray, C.B. Charge transport in strongly coupled quantum dot solids. *Nat. Nanotechnol.* **2015**, *10*, 1013–1026. [CrossRef]
29. Boles, M.A.; Ling, D.; Hyeon, T.; Talapin, D.V. The surface science of nanocrystals. *Nat. Mater.* **2016**, *15*, 364. [CrossRef]
30. Garcia de Arquer, F.P.; Talapin, D.V.; Klimov, V.I.; Arakawa, Y.; Bayer, M.; Sargent, E.H. Semiconductor quantum dots: Technological progress and future challenges. *Science* **2021**, *373*, eaaz8541. [CrossRef]

Disclaimer/Publisher's Note: The statements, opinions and data contained in all publications are solely those of the individual author(s) and contributor(s) and not of MDPI and/or the editor(s). MDPI and/or the editor(s) disclaim responsibility for any injury to people or property resulting from any ideas, methods, instructions or products referred to in the content.